crystals

MDPI

Article

LTCC Ceramic Integration of an Ultra-Wideband High-Pass Filter Chip with Notch Suppression

Chengchao Lv [1,†], Xianglu Shan [1,†], Xinjiang Luo [1,*], Kaixin Song [1,*], Xiaopei Deng [1], Xuan Xie [1] and Changwei Luo [2]

[1] School of Electronics and Information, Hangzhou Dianzi University, Hangzhou 310018, China; 23040629@hdu.edu.cn (C.L.); 15155817041@163.com (X.S.); dengxiaopei2025@163.com (X.D.); 19817102049@163.com (X.X.)
[2] Jiaxing Jiali Electronics Co., Ltd., Jiaxing 314033, China; luochangwei@bdstar.com
* Correspondence: luoxj@hdu.edu.cn (X.L.); kxsong@hdu.edu.cn (K.S.)
† These authors contributed equally to this work.

Abstract

This paper presents a miniaturized ultra-wideband high-pass filter integrated with a notch function based on low-temperature co-fired ceramic (LTCC). The design motivation is to realize continuous wideband high-pass transmission while rejecting a narrow in-band interference/leakage component in compact RF front-end modules. The proposed design employs a cascaded structure of a seventh-order quasi-elliptic HPF and a three-section $\lambda/4$ stub notch filter in a single multilayer LTCC chip. Multiple transmission zeros (TZs) are introduced to improve the lower-stopband selectivity, while the three-section coupled-line NF produces a tunable localized rejection band. The LTCC implementation further integrates multilayer capacitors, three-dimensional helical inductors, shielded strip-line coupling stubs, a grounding compensation capacitor, and an isolation wall to balance compactness, impedance matching, and parasitic suppression. The fabricated chip achieves an ultra-wide bandwidth of 2.35 octaves, a notch 20 dB FBW of 8.5%, an insertion loss below 2 dB, a 60 dB roll-off rate of 154.1 dB/GHz within the lower stopband, and a voltage standing wave ratio (VSWR) less than 2. Experimental results validate that the proposed compact chip meets communication requirements and is suitable for 5G base stations, radar systems, and other applications. The chip dimensions are 4.5 mm × 3.2 mm × 2.5 mm.

Keywords: LTCC; lumped circuit; notch filter; transmission zeros; ultra-wideband high-pass filter

Check for updates

Academic Editor: Raghvendra Singh Yadav

Received: 22 May 2026
Revised: 26 June 2026
Accepted: 29 June 2026
Published: 1 July 2026

Copyright: © 2026 by the authors. Licensee MDPI, Basel, Switzerland. This article is an open access article distributed under the terms and conditions of the Creative Commons Attribution (CC BY) license.

1. Introduction

With the development of 5G/5G-Advanced communication, radar, and broadband RF receiver systems, compact passive front-end filters are required to provide low insertion loss, strong out-of-band suppression, and high integration density [1]. LTCC technology is attractive for these requirements because it supports multilayer routing, embedded lumped elements, vertical interconnection, and compact three-dimensional integration with good RF reliability [2–5].

In broadband receiver chains, the desired signal may occupy a continuous high-frequency band, whereas low-frequency clutter generated by frequency conversion must be suppressed. Therefore, an ultra-wideband (UWB) high-pass response is required rather than a conventional narrowband band-pass response [6–8]. Existing LTCC high-pass filters (HPFs) mainly focus on low-frequency suppression and miniaturization [9,10]; while the

low-frequency spectrum is almost fully occupied, HPF designs need a high-order quasi-elliptic function model to achieve IL below 2 dB, strong rejection exceeding 60 dB, and excellent selectivity for the proper functioning of communication systems [11].

Another practical issue is local-oscillator (LO) leakage. In the intermediate-frequency chain of the X-band meteorological monitoring receiver, the HPF is located after the mixer, serving to filter out low-frequency clutter generated by down-conversion. When the isolation from the LO port to the RF port of the mixer is insufficient, the LO signal within the passband of the HPF will leak into the signal chain, causing electromagnetic interference. Adding a band-stop filter (BSF) directly at the LO source will introduce LO phase noise degradation, while cascading a BSF after the HPF can accurately suppress leakage without affecting the purity of the LO signal. Although researchers have proposed various solutions for BSFs, these works do not fully address the co-integration of UWB HPF transmission and localized notch rejection within a compact LTCC chip. For example, refs. [12–14] proposed electrically coupled compact BSFs, which exhibited low suppression at the stopband center frequency and a wide stopband. Ref. [15] improved these shortcomings using T-shaped transmission-line-connected open stubs, but the centimeter-scale planar footprint hinders miniaturized system integration and applications. The dual-band band-pass filter proposed in [16] exhibits a 20 dB stopband width of 1.2 GHz and demonstrates poor clutter selectivity. Ref. [17] proposed a novel stripline-based wideband BSF, but millimeter-scale dimensions introduce significant parasitic effects, limiting suppression at the stopband center frequency to below 30 dB.

The main contribution of this work is therefore not a single isolated performance metric, but a compact multifunctional LTCC filter architecture that combines UWB high-pass filtering and localized notch rejection in one chip. Specifically, a seventh-order quasi-elliptic lumped-element HPF is used to generate multiple low-frequency transmission zeros (TZs) and steep selectivity exceeding 154.1 dB/GHz, while a three-section $\lambda/4$ parallel-coupled-line notch filter (NF) is introduced to generate one central and two side TZs around the target notch band, which achieves a 20 dB FBW of 8.5%, and a maximum rejection of more than 31 dB near the notch center frequency. A grounding compensation capacitor and an isolation wall are introduced to improve impedance matching and reduce undesired coupling between the HPF and NF sections. Compared with simply cascading two discrete filters, the proposed LTCC integration provides a compact single-chip solution while maintaining competitive insertion loss, stopband suppression, notch rejection, and overall volume.

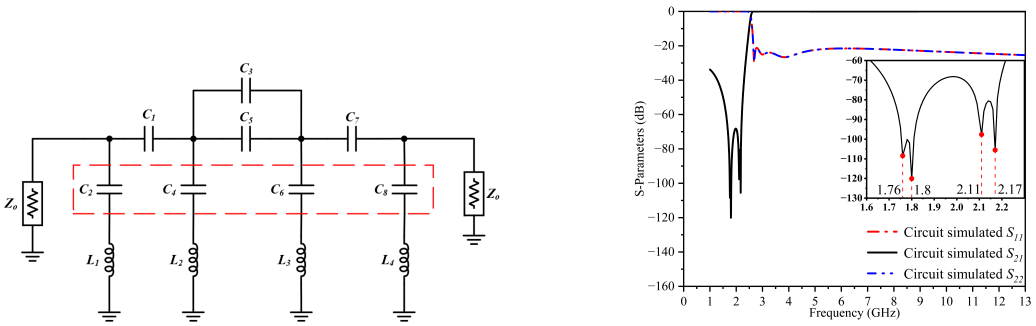
2. Design and Simulation

Based on the application requirement discussed above, the proposed filter is designed as two cascaded functional blocks: a seventh-order quasi-elliptic HPF for UWB transmission and low-frequency clutter suppression, followed by a three-section $\lambda/4$ coupled-line NF for localized in-band interference rejection. This section first describes the circuit-level HPF and NF design, and then explains how the circuit topology is transformed into a multilayer LTCC implementation.

The main design target of the proposed filter is defined as follows: the lower cutoff frequency of the high-pass response is 2.56 GHz; the useful high-pass band should maintain an IL below 2 dB and a VSWR below 2, except for the intentionally introduced notch band; the low-frequency stopband around 2.2–2.3 GHz should provide suppression higher than 30 dB; the center frequency of the notch is 8 GHz where the suppression depth is greater than 30 dB, the localized notch band should cover 7.65–8.25 GHz under the 20 dB rejection criterion; and the overall filter should be implemented in a compact LTCC chip.

2.1. High-Pass Filter Lumped Circuit

The designed ultra-wideband high-pass filter topology is illustrated in Figure 1a. The initial element values were derived from an elliptic-function-inspired prototype, and the circuit was subsequently optimized as a quasi-elliptic HPF with independently controlled transmission zeros (TZs). Unlike a canonical elliptic filter with a standard equiripple stopband response, the proposed circuit employs four series LC resonant branches to generate finite TZs at specified frequencies. These independently positioned TZs improve the transition sharpness and low-frequency stopband suppression while maintaining a compact LTCC implementation and favorable return-loss performance in the high-frequency passband.



(**a**) (**b**)

Figure 1. (**a**) Circuit topology of an HPF with independent TZs. The red dashed box highlights the added shunt capacitors C_2, C_4, C_6, and C_8. Together with inductors L_1, L_2, L_3, and L_4, respectively, they form four series LC resonant branches, thereby introducing four independent transmission zeros and improving the lower-stopband selectivity. The optimized values are $C_1 = 1.1175$ pF, $C_2 = 1.8101$ pF, $C_3 = 0.6677$ pF, $C_4 = 2.0542$ pF, $C_5 = 0.6106$ pF, $C_6 = 1.9074$ pF, $C_7 = 1.2083$ pF, $C_8 = 1.9655$ pF, $L_1 = 4.3143$ nH, $L_2 = 2.7778$ nH, $L_3 = 2.8219$ nH, and $L_4 = 4.1457$ nH; (**b**) *S*-parameter simulation results of the UWB HPF.

This work selects 2.3 GHz as the frequency corresponding to the minimum stopband attenuation ($A_{\min}$) and places the four transmission zeros approximately symmetrically around 1.95 GHz through multiple optimization iterations. The resonant frequency corresponding to the TZs can be calculated using Equation (1). The resonant frequencies corresponding to the inductors from left to right in the design schematic are $f_1 = 1.8$ GHz, $f_2 = 2.11$ GHz, $f_3 = 2.17$ GHz, and $f_4 = 1.76$ GHz.

$$f_i = \frac{1}{2\pi\sqrt{L_i C_{2i}}}, \qquad i = 1, 2, 3, 4 \tag{1}$$

Here, L_i denotes the inductance of the ith series LC branch, while C_{2i} denotes its corresponding capacitance; namely, $C_{2i} = C_2, C_4, C_6$, and C_8 for $i = 1, 2, 3, 4$, respectively.

The parameter values, initially calculated using elliptic-function filter synthesis theory [18–20], were then optimized over multiple iterations in HFSS, as shown in Figure 1. The *S*-parameter simulation results are illustrated in Figure 1b. The resonance of the circuit generates four TZs within the stopband, achieving out-of-band suppression greater than 68 dB and RL exceeding 20 dB in the passband.

2.2. Notch Filter Design

The NF structure, composed of three cascaded TLs, is illustrated in Figure 2. TL1 and TL3 can be regarded as a symmetric coupled transmission line: one line serves as the main transmission path, and the other acts as a coupled resonant branch. Let the physical length of the coupled line unit be l_1, and its electrical length is defined as θ_1.

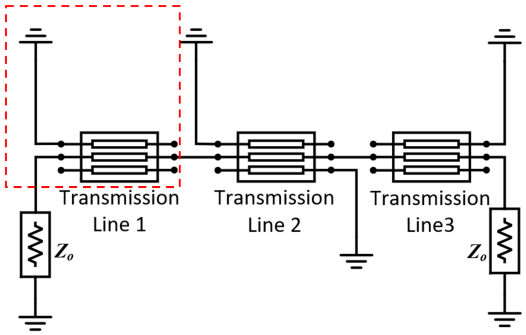


Figure 2. Circuit topology of the NF. The red dashed box highlights Transmission Line 1 (TL1), which is used as the representative coupled-line section in the theoretical analysis; TL3 has the same symmetric configuration.

$$\theta_1 = \beta_1 l_1 \tag{2}$$

Further definition:

$$Y_{p1} = \frac{Y_{0e1} + Y_{0o1}}{2}, \qquad Y_{m1} = \frac{Y_{0e1} - Y_{0o1}}{2} \tag{3}$$

where Y_{p1} denotes the average modal admittance, and Y_{m1} represents the coupling strength.

For the structure, the two terminals of the main transmission line are defined as Port 1 and Port 2, and the two terminals of the coupled branch are defined as Port 3 and Port 4. Here, $V_3 = 0$, $I_4 = 0$. Therefore, the transmission coefficient can be converted from the admittance matrix [17].

$$S_{21} = -\frac{2Y_0 Y_{21}}{(Y_0 + Y_{11})(Y_0 + Y_{22}) - Y_{12}Y_{21}} \tag{4}$$

Here,

$$Y_{11} = j\left(-Y_{p1}\cot\theta_1 + \frac{Y_{m1}^2}{Y_{p1}}\csc\theta_1 \sec\theta_1\right)$$

$$Y_{22} = -j\frac{Y_{p1}^2 - Y_{m1}^2}{Y_{p1}}\cot\theta_1$$

$$Y_{21} = j\frac{Y_{p1}^2 - Y_{m1}^2}{Y_{p1}}\csc\theta_1$$

Therefore, the condition for the generation of TZ is

$$f_Z = \frac{c}{4l_1\sqrt{E_{\text{eff}}}} \tag{5}$$

$$f_Z = f_0, \qquad \left(l_1 = \frac{\lambda}{4}\right) \tag{6}$$

The TL2 consists of a main line and two $\lambda/4$ stubs located on the upper and lower sides of the main line, with the grounding terminals of two stubs facing in opposite directions. For TL2, the branch resonant network is written as

$$Y_r = j\begin{bmatrix} -Y_{p2}\cot\theta_2 & Y_{m2}\csc\theta_2 \\ Y_{m2}\csc\theta_2 & -Y_{p2}\cot\theta_2 \end{bmatrix} \tag{7}$$

The TZs of TL2 correspond to the eigen-resonance condition of the coupled resonant network. Therefore, the condition for the generation of TZs is

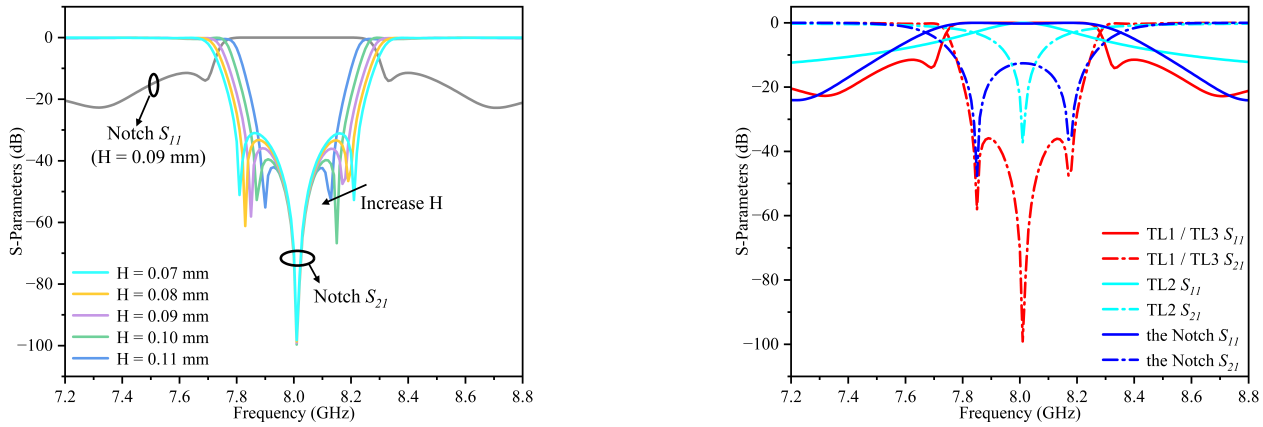
$$\cos\theta_2 = \pm\frac{Y_{m2}}{Y_{p2}} = \pm k_2 \tag{8}$$

where k_2 is the equivalent coupling coefficient. Therefore, the frequencies of the two TZs for TL2 are

$$f_Z = f_0\left(1 \pm \frac{2}{\pi}\sin^{-1}k_2\right), \qquad \left(l_2 = \frac{\lambda}{4}\right) \tag{9}$$

It is demonstrated that the two TZs of the TL2 are mainly determined by k_2.

The line width and spacing of the NF were iteratively optimized using ADS. Considering the impedance-matching and layout constraints, the physical length, width, and conductor thickness of the transmission lines were determined as $L = 3.145$ mm, $W = 0.116$ mm, and $T = 0.01$ mm, respectively. Figure 3a shows that as the vertical spacing H between the coupled stubs increases, the coupling strength decreases and the notch bandwidth narrows, which is consistent with the theoretical analysis. Finally, H was set to 0.09 mm.



(**a**) (**b**)

Figure 3. (**a**) Stopband response at different H; (**b**) frequency response of the NF and each TL section.

As shown in Figure 3b, TL1 and TL3 generate a TZ at 8.01 GHz with a rejection depth of 37.3 dB. TL2 generates two TZs at 7.85 and 8.17 GHz, which are approximately symmetric about 8.01 GHz, with rejection levels of 47.6 and 36.3 dB, respectively. The symmetric NF structure achieves attenuation levels of 58.1, 99.096, and 47.49 dB at the three TZ frequencies within a 420 MHz-wide 20 dB stopband.

The simulated S-parameter response of the ideal HPF–NF circuit model is shown in Figure 4. The theoretical suppression exceeds 30 dB from 7.83 to 8.20 GHz, with a theoretical notch depth of approximately 130 dB at 8.01 GHz. However, this value represents the ideal transmission-zero response of the circuit model rather than the practical rejection level after LTCC implementation and fabrication.

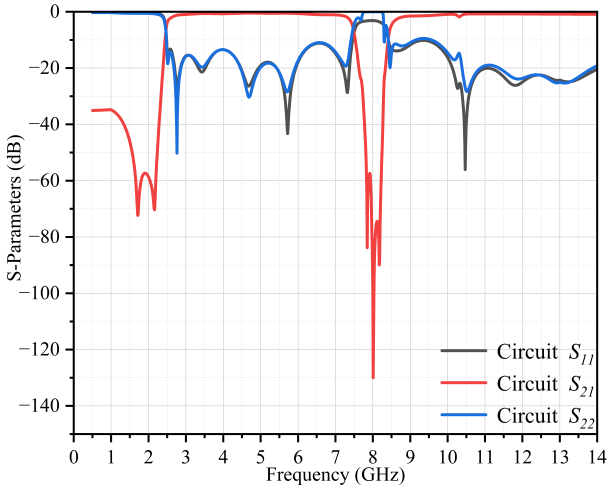


Figure 4. Frequency response of the HPF cascaded with the NF.

3. 3D Modeling

This work employs HFSS electromagnetic simulation software to design and analyze a three-dimensional (3D) model of the UWB HPF integrated with notch functionality. The LTCC process uses L751 green tapes developed by Jiaxing Jiali Electronics Co., Ltd., Jiaxing, China, with available tape thicknesses of 15, 20, 25, 30, 35, 40, 45, and 60 μm; a relative permittivity of $\varepsilon_r = 7.5$; a loss tangent of $\tan\delta = 0.003$; and a shrinkage rate of 21.12%. The lamination parameters are 80 °C, 35 MPa, a preheating time of 500 s, and a holding time of 500 s. The internal conductors, external pads, vias, and ground structures were fabricated using a silver-based conductor paste, and the vias were filled with the same conductive paste. In the HFSS model, these conductive structures were represented using silver metallization. The fired conductor thickness and via diameter are 0.01 mm and 0.04 mm, respectively. These process-related parameters are provided to improve the reproducibility of the LTCC implementation. The internal structure is illustrated in Figure 5a.

The dimensions of each component are illustrated in Figure 5. Layers 1–10 are dedicated to the UWB HPF, whereas Layers 11–21 are used for the NF. The layers are interconnected through vias. The capacitors are implemented using multilayer vertical interdigital capacitor structures, while the inductors are realized as three-dimensional multi-turn helical structures. Small capacitors in LTCC filters exhibit more stable equivalent capacitance in the high-frequency range, thereby improving the VSWR performance. Therefore, two parallel small capacitors, C_3 and C_5, were implemented on the same plane. Capacitors C_3 and C_5 are connected in parallel and jointly provide the required equivalent capacitance in the main signal path, thereby contributing to impedance matching and passband-response control. This arrangement not only fully utilizes the flexible multilayer stacking capability of LTCC technology but also partially compensates for parasitic inductance, as shown in Figure 6a.

The layout of the decoupling capacitor C_9 to ground in the 3D model is shown in Figure 5a. To quantitatively evaluate the effects of C_9 and the Isolation Wall, the key simulated performance metrics before and after introducing these two structures are compared in Figure 6a,b and Table 1. Without C_9 and the Isolation Wall, the cascaded HPF–NF structure suffers from impedance mismatch caused by the discontinuity between the lumped HPF section and the strip-line NF section. As a result, the passband RL deteriorates and the VSWR increases. After introducing C_9 and the Isolation Wall, the passband IL is maintained below 2 dB, the RL is improved to more than 12 dB, the VSWR is reduced to below 2, and the notch suppression remains greater than 35 dB. This confirms that C_9 provides

capacitive compensation for impedance matching, while the Isolation Wall suppresses parasitic electromagnetic coupling between the HPF and NF.

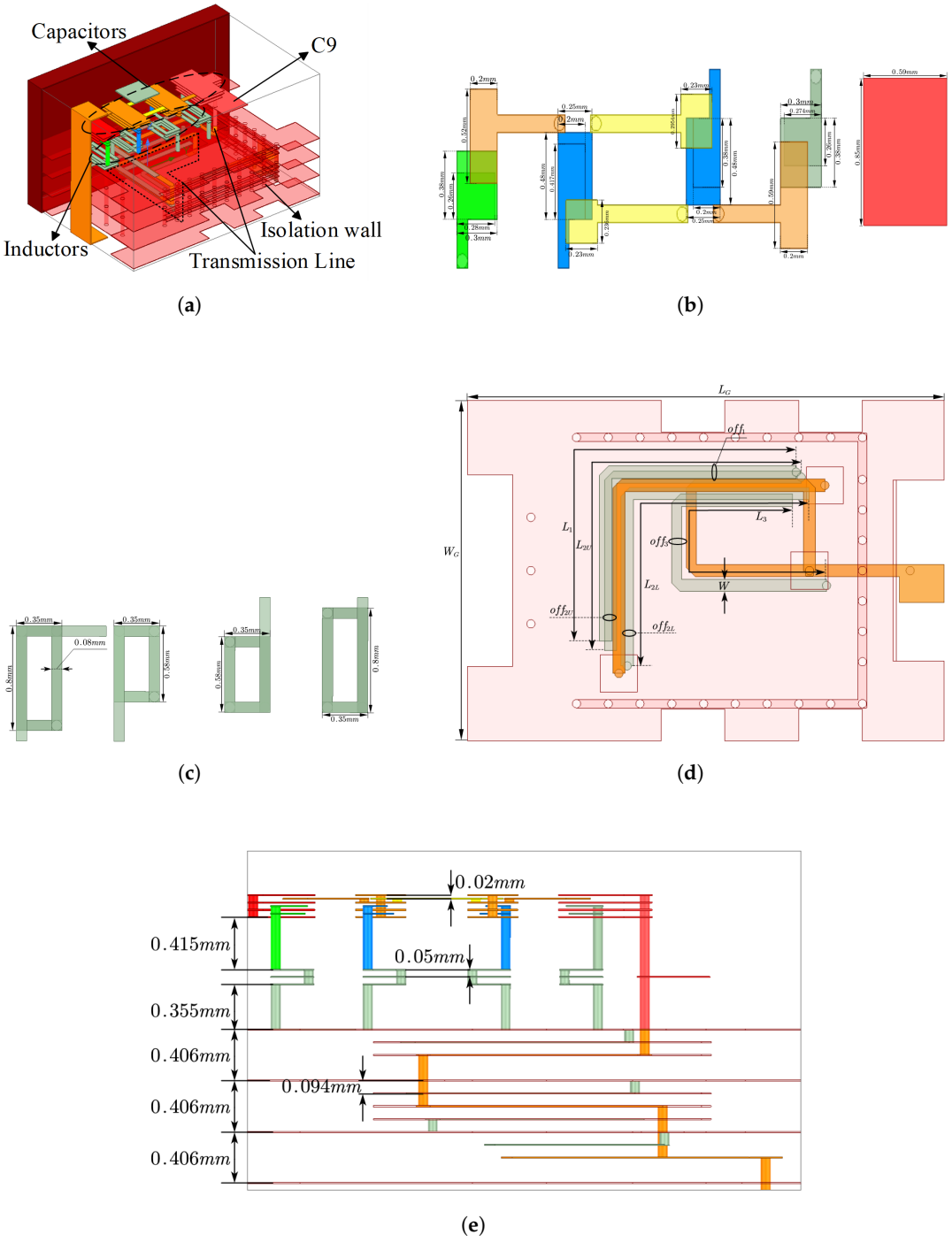
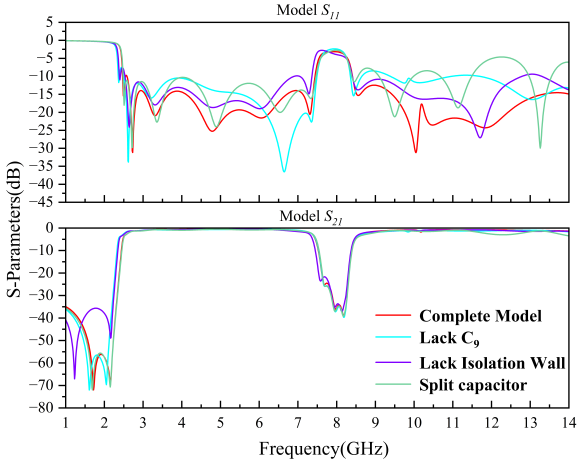
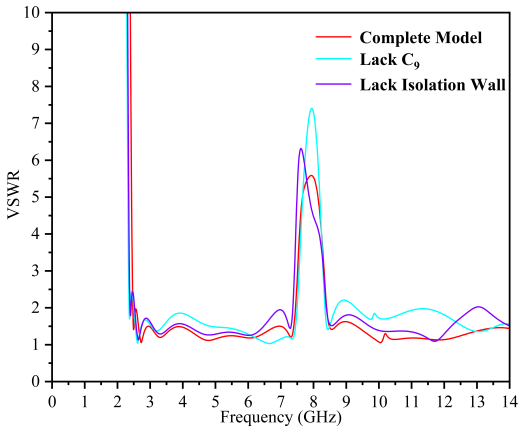


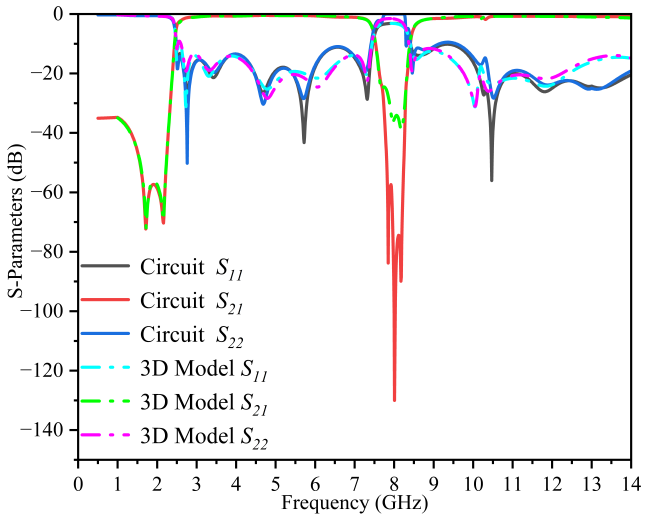
Figure 5. (**a**) 3D model including capacitor C_9 and the isolation wall; (**b**) dimensions of the capacitive substrates; (**c**) dimensions of the inductive substrates; (**d**) dimensions of the transmission lines and ground substrates. The optimized dimensions are $W_G = 3.2$ mm, $L_G = 4.5$ mm, $L_1 = L_{2U} = L_{2L} = L_3 = 3.145$ mm, $W = 0.1$ mm, $\text{off}_1 = 0.125$ mm, $\text{off}_{2U} = \text{off}_{2L} = 0.078$ mm, and $\text{off}_3 = 0.139$ mm; (**e**) substrate layer diagram.



(**a**)



(**b**)



(**c**)

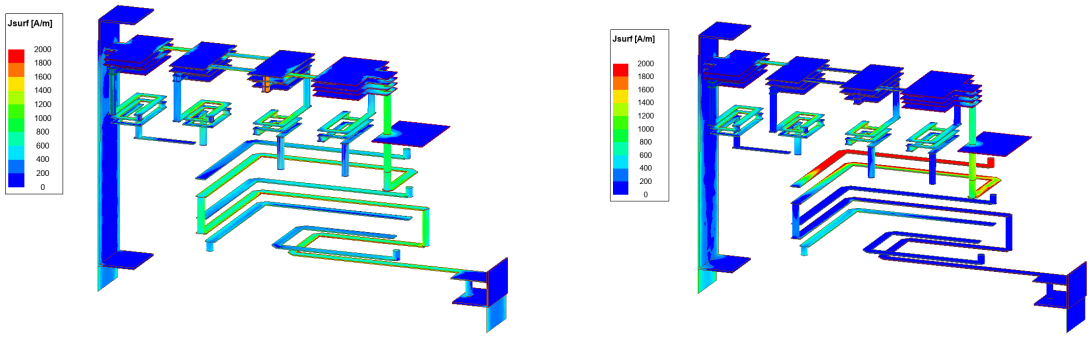
Figure 6. (**a**) Performance comparison of each model optimization method; (**b**) VSWR comparison; (**c**) frequency response comparison between the theoretical circuit model and the 3D model.

Table 1. Quantitative effects of capacitor C_9 and isolation wall.

Structure	Complete Model	Lack C_9	Lack Isolation Wall
Maximum IL (dB)	1.75	1.73	1.29
Minimum RL (dB)	12.46	8.49	9.86
Maximum VSWR	1.62	2.21	1.95
Cutoff frequency (GHz)	2.56	2.47	2.49
Notch suppression (dB)	35.47	36.47	34.06
20 dB notch bandwidth (MHz)	680	700	760

After circuit-to-layout transformation, the 3D model was further optimized in HFSS by tuning the coupling spacing, via connections, grounding structures, and local layout details. As shown in Figure 6c, the 3D model maintains an IL below 2 dB and an RL greater

than 12 dB, with notch-band suppression exceeding 30 dB. However, compared with the ideal circuit model, the notch depth of the 3D model is reduced because of radio-frequency (RF) parasitic effects. Conductor loss, dielectric loss, via parasitic inductance, interlayer coupling, and the finite quality factor of the stripline resonator collectively weaken the notch suppression. The surface-current distributions in Figure 7 further demonstrate that the current paths at 5 GHz and 8 GHz are different. At 8 GHz, the coupled short-circuited stub in TL1 reaches its $\lambda/4$ resonant condition. The RF energy is strongly coupled from the main line into the short-circuited branch, forming a current maximum near the short-circuited end. Consequently, the local surface current density is substantially higher than that at 5 GHz. This current concentration confirms that the notch response originates from the resonant loading effect of the coupled short-circuited transmission-line section.



(**a**) (**b**)

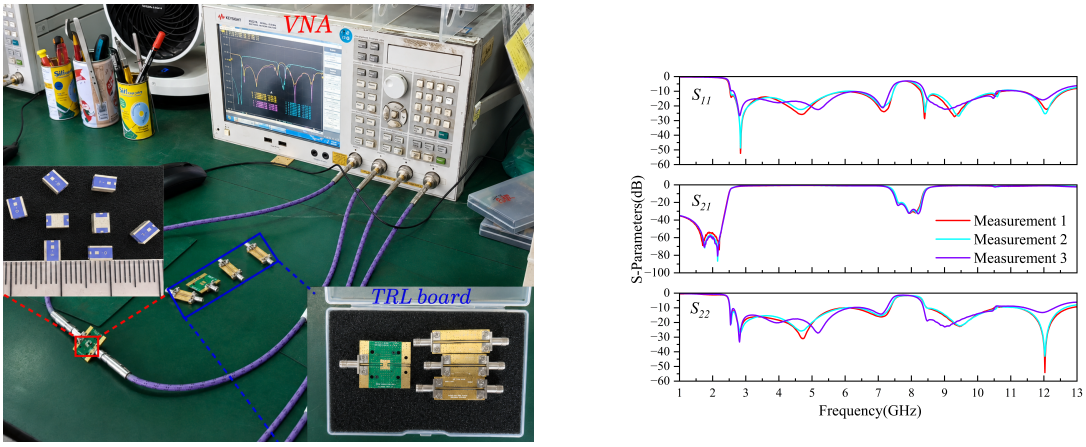
Figure 7. Scalar distributions of the surface current density using the same color scale of 0–2000 A/m: (**a**) simulation frequency of 5 GHz and phase of 0°; (**b**) simulation frequency of 8 GHz and phase of 0°.

4. Results and Analysis

The fabricated UWB HPF chip integrated with notch functionality is shown in Figure 8a. The LTCC chip was soldered onto the PCB test fixture through its coplanar signal and ground pads rather than being measured using direct coplanar probing. The *S*-parameters were measured using a Keysight E5071C vector network analyzer with through-reflect-line (TRL) calibration over the frequency range of 0–20 GHz. The TRL calibration reference planes were established at the PCB solder pads adjacent to the input and output terminals of the LTCC chip. Therefore, the test cables, SMA connectors, and PCB transition lines preceding these pads were de-embedded. A successful calibration was verified using the Through standard, for which $S_{11} < -50$ dB and $S_{21} > -0.2$ dB were obtained. Because the solder joints cannot be removed by the calibration, the measured response includes the LTCC chip, the solder joints, and the residual parasitic effects near the chip-to-PCB interfaces. The sampling repeatability results for multiple devices from the same fabrication batch are shown in Figure 8b. Although slight variations are observed in the return loss, the devices exhibit consistent low-frequency transmission-zero locations, notch rejection, and passband insertion loss.

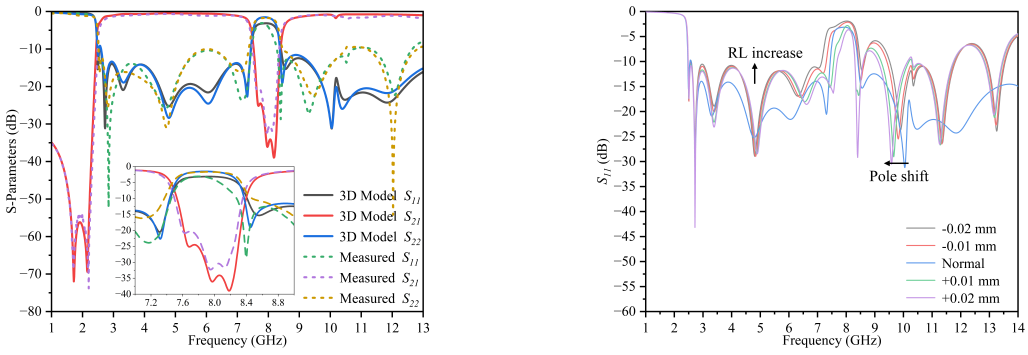
As shown in Figure 9a, within the notch band of 7.60–8.28 GHz, the suppression level exceeds 20 dB, with a maximum suppression of more than 31 dB near the center frequency. The passband IL remains below 2 dB, and the low-frequency stopband suppression from 2.2 to 2.3 GHz exceeds 30 dB. The proposed filter also exhibits four TZs and a VSWR below 2. The measured results show a slight shift of the transmission pole from approximately 10 GHz to 9.33 GHz, together with a deterioration in the passband return loss. These discrepancies are mainly attributed to dimensional variations introduced during the LTCC sintering process. As shown in Figure 9b, the vertical coupling spacing H was varied by

$\Delta H = -0.02, -0.01, 0, +0.01$, and $+0.02$ mm to evaluate the influence of shrinkage-induced dimensional deviations. Variations in H alter the coupling capacitance and consequently shift the high-frequency transmission poles and change the return-loss response.



(**a**) (**b**)

Figure 8. (**a**) Photograph of the fabricated chip and measurement setup; (**b**) repeatability measurements.



(**a**) (**b**)

Figure 9. (**a**) Comparison of the simulated and measured S-parameter responses; (**b**) influence of variations in the vertical coupling spacing H, where $\Delta H = -0.02, -0.01, 0, +0.01$, and $+0.02$ mm.

In Table 2, the cascaded HPF is listed as a seventh-order filter, whereas in Table 3, "3 sections" refers to the three coupled-line sections of the NF.

Tables 2 and 3 present comparisons of the performance and dimensions of this work with those of similar existing works. The main advantage of the proposed design over the reported filters is the integration of high-pass filtering and notch suppression within a compact LTCC chip while maintaining competitive ultra-wide bandwidth, IL, stopband suppression, narrow stopband, and size. These comparisons emphasize the comprehensive advantages of multifunctional integration, compact implementation, and balanced filtering performance rather than the absolute advantage of a single parameter.

Table 2. Comparison of HPF performance and size with previously reported designs. Here, selectivity denotes the 60 dB roll-off rate.

Ref.	Type	Technology	Order	Octaves	Selectivity (dB/GHz) @(GHz)	IL (dB)	RL (dB)	Size (mm × mm × mm)
[9]	Highpass	LTCC	7	0.82	20.1@7.58	<3.1	>10	3.2 × 1.6 × 1
[10]	Highpass	LTCC	9	0.71	40.1@7.92	<1.05	>10	10 × 9.86 × 1
This work	Highpass	LTCC	7	2.35	154.1@2.56	<2	>10	4.5 × 3.2 × 2.5

Table 3. Comparison of NF performance and size with similar reported designs.

Ref.	Type	Technology	ε_r	tan δ	Order/Sections	20 dB FBW	Size (mm × mm × mm)
[12]	Dual-Band Bandstop	SSL	2.2	–	2	12.1% 7.2%	30 × 20 × 18.8
[14]	Bandstop	LTCC	5.9	0.002	2	24.7%	3.3 × 2.85 × 2
[16]	Bandstop	LTCC	6.64	0.008	7	34.3%	2.7 × 2.3 × 0.68
[17]	Bandpass-Notch	LTCC	7.8	–	4	12.7%	3 × 6.3 × 0.45
This work	Notch	LTCC	7.5	0.003	3 sections	8.5%	4.5 × 3.2 × 2.5

5. Conclusions

This work proposes a miniaturized LTCC UWB HPF integrated with a localized notch function. The design combines a seventh-order quasi-elliptic lumped-element HPF and a three-section $\lambda/4$ coupled-line NF in a single multilayer LTCC chip. The quasi-elliptic HPF provides multiple low-frequency TZs and steep lower-stopband suppression, while the coupled-line NF introduces a measured 20 dB notch band of 7.6–8.28 GHz and a maximum rejection exceeding 31 dB near the notch center frequency. The grounding compensation capacitor C_9 improves the impedance matching of the cascaded HPF–NF network, and the isolation wall reduces undesired coupling between the lumped and distributed sections. The fabricated chip achieves a cutoff frequency of 2.56 GHz, a frequency ratio of 5.08 corresponding to 2.35 octaves, passband IL below 2 dB, low-frequency suppression higher than 30 dB from 2.2 to 2.3 GHz, and VSWR below 2. With a compact size of 4.5 mm × 3.2 mm × 2.5 mm, the proposed design demonstrates a balanced integration of UWB high-pass filtering and localized notch rejection for compact broadband RF front-end applications.

Author Contributions: Conceptualization, C.L. (Chengchao Lv) and X.L.; methodology, C.L. (Chengchao Lv); software, C.L. (Chengchao Lv) and X.S.; validation, C.L. (Chengchao Lv), X.S. and X.D.; formal analysis, C.L. (Chengchao Lv); investigation, C.L. (Chengchao Lv); resources, X.L., K.S. and C.L. (Changwei Luo); data curation, C.L. (Chengchao Lv); writing—original draft preparation, C.L. (Chengchao Lv); writing—review and editing, X.L., X.S. and K.S.; visualization, C.L. (Chengchao Lv) and X.X.; supervision, X.L. and K.S.; project administration, X.L.; funding acquisition, X.S. and X.L. All authors have read and agreed to the published version of the manuscript.

Funding: This research was funded by the Xinmiao Program of Zhejiang Province, grant number 2025R407C065.

Institutional Review Board Statement: Not applicable.

Informed Consent Statement: Not applicable.

Data Availability Statement: The data presented in this study are available on request from the corresponding authors.

Acknowledgments: The authors would like to thank the members of the research group for their valuable discussions and technical support.

Conflicts of Interest: Author Changwei Luo is employed by Jiaxing Jiali Electronics Co., Ltd. The remaining authors declare that the research was conducted in the absence of any commercial or financial relationships that could be construed as a potential conflict of interest.

References

1. Chen, L.; Liu, H.; Jiang, Y.; Li, S.; Luo, X.; You, B.; Li, A.; Hu, Y.; Baxter, H.; Yang, B.; et al. High quality of $LiMg_{0.9}Zn_{0.06}Ni_{0.04}PO_4$-$TiO_2$ microwave ceramic and its application for 5G dielectric waveguide bandpass filter. *Mater. Today Commun.* **2023**, *35*, 105500.
2. Jiang, Y.; Liu, H.; Muhammad, R.; Luo, X.; Song, K.; Mao, M.; Sun, S.; Bafrooei, H.B.; Taheri-Nassaj, E.; Iqbal, Y.; et al. Broadband and high-efficiency of garnet-typed ceramic dielectric resonator antenna for 5G/6G communication application. *Ceram. Int.* **2022**, *48*, 26922–26927.

3. Zhao, W.; Wu, Y.; Yang, Y.; Wang, W. LTCC bandpass filter chips with controllable transmission zeros and bandwidths using stepped-impedance stubs. *IEEE Trans. Circuits Syst. II Express Briefs* **2022**, *69*, 2071–2075. [CrossRef]
4. Xing, M. Modeling and Research of Radio Frequency Passive Devices Based on LTCC Technology. Ph.D. Thesis, Xidian University, Xi'an, China, 2012.
5. Deng, Y. Research on Microwave Passive Components Based on LTCC Technology. Master's Thesis, Xidian University, Xi'an, China, 2014.
6. Ebrahimi, A.; Ghorbani, K. UHF bandpass filter using a combination of semi-lumped and lumped components. In Proceedings of the 2023 Asia-Pacific Microwave Conference (APMC), Taipei, Taiwan, 5–8 December 2023; pp. 682–684.
7. Xu, B.; Yang, C.; Chen, P.; Wang, H.; Zong, X.; Sun, S. A miniaturized and packaged LTCC filtering balun using lumped elements. In Proceedings of the 2022 IEEE MTT-S International Microwave Workshop Series on Advanced Materials and Processes for RF and THz Applications (IMWS-AMP), Guangzhou, China, 27–29 November 2022; pp. 1–2.
8. Pourzadi, A.; Adibi, A.; Mousavi, S.H.; Kouki, A. A fast technique for realization of lumped-element values into 3-D physical layout on LTCC. *IEEE Trans. Compon. Packag. Manuf. Technol.* **2021**, *11*, 1497–1505. [CrossRef]
9. Zeng, J.; Huang, K.; Ta, S. A LC resonator based high-pass filter embedded in LTCC substrate. In Proceedings of the 2022 IEEE MTT-S International Microwave Workshop Series on Advanced Materials and Processes for RF and THz Applications (IMWS-AMP), Guangzhou, China, 27–29 November 2022; pp. 1–2.
10. Tao, M.-C.; Wu, Y.-W.; Hao, Z.-C.; Gao, L.; Wang, J.; Wang, X. Design of a miniature high-pass filter using LTCC technology. In Proceedings of the 2018 International Applied Computational Electromagnetics Society Symposium—China (ACES), Beijing, China, 29 July–1 August 2018; pp. 1–2.
11. Huo, X.; Wang, P. A miniaturized high out-band suppression low-pass filter based on the lumped circuit model using LTCC technology. In Proceedings of the 2012 International Conference on Computational Problem-Solving (ICCP), Leshan, China, 19–21 October 2012; pp. 271–274.
12. Yu, Z.; Xu, L.; Liu, C. Design of a suspended stripline dual-band band-stop filter loaded with short-ended waveguide stubs embedded in the metal housing. *IEEE Microw. Wirel. Compon. Lett.* **2020**, *30*, 1025–1028.
13. Lee, H.-S.; Lim, W.-G.; Kim, C.-Y. Bandstop resonator using electrically coupled open stub for compact wideband bandstop filters. In Proceedings of the 2013 Asia-Pacific Microwave Conference (APMC), Seoul, Republic of Korea, 5–8 November 2013; pp. 963–965.
14. Wu, D.-S.; Li, Y.C.; Hu, B.-J. LTCC wideband bandstop filter with controllable bandwidth using internal coupling. In Proceedings of the 2019 International Conference on Microwave and Millimeter Wave Technology (ICMMT), Guangzhou, China, 19–22 May 2019; pp. 1–3.
15. Zhang, T.; Bao, J.; Cai, Z. Compact bandstop filter with high stopband attenuation. In Proceedings of the 2017 IEEE MTT-S International Microwave Symposium (IMS), Honolulu, HI, USA, 4–9 June 2017; pp. 1916–1918.
16. Park, J.H.; Cheon, S.J.; Park, J.Y.; Lim, J.T. Ultra-compact dual-band WLAN filter using independent band stop resonators. In Proceedings of the 2011 IEEE 61st Electronic Components and Technology Conference (ECTC), Lake Buena Vista, FL, USA, 31 May–3 June 2011; pp. 2096–2100.
17. Duong, T.H.; Kim, I.S. Wideband bandstop filter based on capacitively coupled $\lambda/4$ short-circuited lines. *J. Electromagn. Eng. Sci.* **2010**, *10*, 92–98. [CrossRef]
18. Alexandru, I.M.; Viman, L.; Pitică, D. Implementation of a microwave elliptical low pass filter with radial stubs. In Proceedings of the 2016 IEEE 22nd International Symposium for Design and Technology in Electronic Packaging (SIITME), Oradea, Romania, 20–23 October 2016; pp. 59–62.
19. Liu, X.; Liu, D.; Chen, Y.; Zhou, Y.; Tang, Z. Design of gain and bandwidth configurable elliptic low-pass filter. In Proceedings of the 2018 14th IEEE International Conference on Solid-State and Integrated Circuit Technology (ICSICT), Qingdao, China, 31 October–3 November 2018; pp. 1–3.
20. Zhao, P.; Xiong, Z.-A. Fast synthesis of elliptic prototype filters. *IEEE Microw. Wirel. Technol. Lett.* **2023**, *33*, 1127–1130. [CrossRef]

Disclaimer/Publisher's Note: The statements, opinions and data contained in all publications are solely those of the individual author(s) and contributor(s) and not of MDPI and/or the editor(s). MDPI and/or the editor(s) disclaim responsibility for any injury to people or property resulting from any ideas, methods, instructions or products referred to in the content.